

Directivity Enhancement and Characteristics of Space-Wave, Leaky-Wave and Creeping-Waves for an Impedance Cylinder Coated with Dielectric

Mahesh Singh¹, Bratin Ghosh^{2*}, Kamal Sarabandi³

¹ Department of Electronics and Electrical Communication Engineering, Indian Institute of Technology, West Bengal, India

³ Department of Electrical Engineering and Computer Science, University of Michigan, Ann Arbor, MI, USA

*bghosh@ece.iitkgp.ac.in

Abstract: The dielectric-coated impedance cylinder configuration is investigated thoroughly with respect to the space-wave, leaky-wave and creeping-wave excitations for all source polarizations. A very high directivity is achieved for the space- and leaky-wave radiation for the antenna structure compared to that from a dielectric cylindrical rod investigated earlier. It is also observed that such high directivity for the dominant-mode leaky-wave is accompanied by higher-order azimuthal harmonics with low attenuation constant contributing to the leaky-wave pole, instead of the $n = 0$ harmonic for the previous configuration. A large enhancement in the space-wave directivity is also achieved, contributed by higher space-wave harmonics compared to lower-order azimuthal harmonics for the cylindrical dielectric rod antenna. The space-wave and leaky-wave directivities are examined with variation in the design parameters and azimuthal harmonics. The phase and attenuation characteristics of the leaky-wave are used to evaluate the optimized leaky-wave structure parameters and appropriate azimuthal harmonics that result in high directivity for the configuration. The creeping-wave characteristics for the configuration are also investigated, with a relatively stronger creeping-wave excitation observed for an inductive surface-impedance.

1 Introduction

Non-planar antenna configurations based on cylindrical structures have attracted research attention in view of their applications in missile bodies, bullet surfaces, aerodynamic structures and borehole in geophysics. Diffraction due to array of dipole antennas placed around the conducting cylinder was investigated in [1] using the reciprocity principle. Diffraction of plane wave due to a conducting cylinder was presented in [2]. The scattered field due to a dipole source in the presence of an infinitely long perfectly conducting cylinder was reported in [3], [4] using the Green's function technique. Formulations related to the scattering of an obliquely incident plane wave incident on a circular dielectric cylinder and far-field radiation patterns due to point sources in the presence of a dielectric cylinder were developed in [5] and [6] respectively.

Gain enhancement of printed antennas in a substrate-superstrate configuration was investigated in [7] while that in a multilayer configuration was treated in [8]. High gain leaky-wave planar printed antenna configurations were also reported using the substrate-superstrate and multilayered structures in [9] and [10], respectively.

Excitation of surface-waves on a dielectric cylinder coated with a circular filament of magnetic current was investigated in [11] for the lowest order TM mode. The effect of different source polarizations, particularly for higher-order modes possessing mode-coupling that contributes significantly to both space-wave and leaky-wave radiation, has not been considered. The creeping, leaky and surface-waves have been investigated in [12] for a dielectric-coated circular cylinder and compared with the leaky and surface-wave propagation for a planar dielectric slab. However, the axial wavenumber k_z has not been considered in the

treatment for the cylindrical configuration in [12]. Characteristics of space-wave, leaky-wave and creeping-waves was investigated in [13] for a dielectric cylinder for different source polarizations. A high space-wave and leaky-wave gain was observed for certain parameter values / source polarizations for the configuration. A high-gain and wide-band conformal leaky-wave microstrip antenna configuration on a coated PEC cylinder was investigated in [14].

In addition to research on PEC and coated PEC objects, the impedance surface both in planar and non-planar forms have attracted research attention. The planar impedance surface has been investigated due to its practical applications in the treatment of the lossy earth that is modeled as a flat impedance surface. The problem of an infinitesimal dipole radiating over a planar impedance surface was formulated in [15]. A reactive impedance surface was proposed in [16] to design a miniaturized patch antenna with enhanced gain, efficiency and bandwidth. The cylindrical impedance surface was also investigated in view of its potential applications in the modeling of the fuselage of an aircraft, spacecraft or a missile [17] or a high building with circular cross-section [18]. A uniform geometrical theory of diffraction (UTD) based asymptotic solution was presented in [17] for the Green's function related to the magnetic field on a circular impedance cylinder excited by a magnetic current source. An approximate solution for the evaluation of the scattered field due to a $\hat{\rho}$, $\hat{\phi}$ and \hat{z} -directed dipole source placed near the finite conducting and finite impedance cylinder was presented in [18]. A UTD-based approach with the effective impedance boundary condition is used to compute the surface fields of a thin-dielectric coated PEC circular cylinder in [19]. Scattering due to obliquely incident plane wave on an electrically large

This is the author manuscript accepted for publication and has undergone full peer review but has not been through the copyediting, typesetting, pagination and proofreading process, which may lead to differences between this version and the Version of Record. Please cite this article as doi: 10.1049/mia2.12038.

impedance cylinder was analyzed using the UTD in [20].

In the following work, the space-wave, leaky-wave and creeping-waves on a dielectric coated impedance cylinder is thoroughly characterized for the $\hat{\rho}$, $\hat{\phi}$ and \hat{z} -directed electric current source located in the cylindrical dielectric layer. The reflection coefficient due to the cylindrical impedance surface is formulated using the impedance boundary condition. Compared to the antenna configuration presented in [13], the current configuration achieves a much higher directivity for the space-wave and leaky-wave. Also, a much higher directivity is achieved compared to the case of the impedance cylinder / thin-dielectric coated PEC cylinder in [17] – [20]. The large enhancement in the leaky-wave directivity in the current case is due to the dominant leaky-wave radiation contributed by the poles due to the reflections in the dielectric-to-impedance surface and dielectric-to-air interfaces, instead of the poles of the transmission matrix in [13]. In addition, the dominant leaky-wave radiation in the current case is contributed by higher-order azimuthal modes compared to $n=0$ in [13] corresponding to lower values of attenuation constant for these higher-order modes. For the space-wave radiation, the significant enhancement in directivity in the current configuration is contributed by higher-order modes compared to the lower order harmonics in [13]. Distinctive features of the creeping-wave for the current antenna configuration are also investigated for all source polarizations.

2. Formulation

Fig. 1 shows the configuration of the impedance cylinder (Region 1) coated with a dielectric layer (Region 2). Region 1 possesses a uniform surface impedance $Z_s = Z'_s + jZ''_s$ with a radius of a_1 . The permittivity and permeability of Region 2 are ϵ_2 and μ_2 respectively with a radius a_2 , with the permittivity and permeability of the outermost layer (Region 3) denoted by ϵ_3 and μ_3 respectively. An $\hat{\alpha}$ -directed electric point source is located in Region 2 at (ρ', ϕ', z') with the observation point P located at (ρ, ϕ, z) in Region 3. A time convention of $e^{j\omega t}$ is adopted in the work.

In order to derive the reflection terms due to the impedance cylinder we consider only Region 1 and Region 2 in Fig. 1 with the $\hat{\alpha}$ -directed electric point source located in Region 2. In this case, the z-component of the electric and magnetic field Green's functions can be written as [21]:

$$\begin{bmatrix} E_{z2} \\ H_{z2} \end{bmatrix} = \frac{1}{2\pi} \int_{-\infty}^{\infty} dk_z e^{-jk_z(z-z')} \sum_{n=-\infty}^{\infty} e^{-jn(\phi-\phi')} \begin{bmatrix} \tilde{E}_{z2} \\ \tilde{H}_{z2} \end{bmatrix} \quad (1)$$

In the above, the spectral electric and magnetic field components \tilde{E}_{z2} and \tilde{H}_{z2} are given by:

$$\begin{bmatrix} \tilde{E}_{z2} \\ \tilde{H}_{z2} \end{bmatrix} = \begin{cases} [J_n(k_{\rho 2} \rho) \cdot \bar{I} + H_n^{(2)}(k_{\rho 2} \rho) \cdot \bar{R}_{21}] \cdot H_n^{(2)}(k_{\rho 2} \rho') \cdot \bar{D}'_2, & \rho < \rho' \\ H_n^{(2)}(k_{\rho 2} \rho) \cdot [J_n(k_{\rho 2} \rho') \cdot \bar{I} + H_n^{(2)}(k_{\rho 2} \rho') \cdot \bar{R}_{21}] \cdot \bar{D}'_2, & \rho > \rho' \end{cases} \quad (2)$$

with

$$\bar{D}'_2 = \frac{-1}{4\omega\epsilon_2} \left[(\hat{z}k_z^2 + jk_z \bar{\nabla}') \cdot \hat{\alpha} \right], \quad k_{\rho 2}^2 = k_2^2 - k_z^2 \quad (3)$$

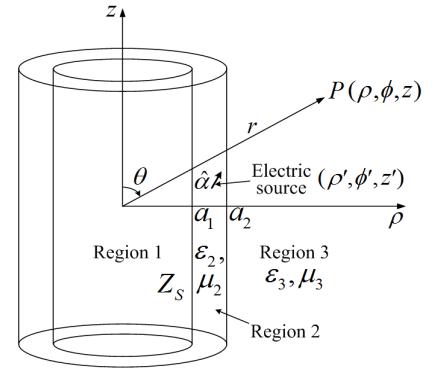


Fig. 1. Impedance cylinder coated with dielectric layer.

In (2), \bar{I} denotes the 2×2 identity matrix, while \bar{R}_{ij} ($i=2, j=1$) is a 2×2 matrix characterizing the local reflection for a wave incident from Region i on the Region i – Region j layer interface. Also, in the above, $H_n^{(2)}(x)$ and $J_n(x)$ are the Hankel function of second kind and Bessel function of first kind of order n , respectively. In (2), the z-directed electric and magnetic fields corresponding to the $\hat{\alpha}$ -directed electric point source in Region 2 are obtained using the operator \bar{D}'_2 . The corresponding transverse electric and magnetic field components can also be obtained from (2).

In order to determine the reflection matrix \bar{R}_{21} , the impedance boundary condition given by [22]:

$$\hat{\rho} \times \vec{E} = Z_s \hat{\rho} \times (\hat{\rho} \times \vec{H}) \quad (4)$$

is applied at $\rho = a_1$.

Eqn. (4) can be written in the spectral domain as:

$$\begin{bmatrix} \tilde{E}_{z2} \\ \tilde{H}_{z2} \end{bmatrix} = \begin{bmatrix} Z_s & 0 \\ 0 & -Z_s^{-1} \end{bmatrix} \begin{bmatrix} \tilde{H}_{\phi 2} \\ \tilde{E}_{\phi 2} \end{bmatrix} = \bar{Z}_s \cdot \begin{bmatrix} \tilde{H}_{\phi 2} \\ \tilde{E}_{\phi 2} \end{bmatrix} \quad (5)$$

Using the expressions for the transverse field components $\tilde{E}_{\phi 2}$ and $\tilde{H}_{\phi 2}$ in (5), we obtain the local reflection matrix due to the impedance cylinder as:

$$\bar{R}_{21} = -[H_n^{(2)}(k_{\rho 2} a_1) \cdot \bar{I} - \bar{Z}_s \cdot \bar{H}_n^{(2)}(k_{\rho 2} a_1)]^{-1} \cdot [J_n(k_{\rho 2} a_1) \cdot \bar{I} - \bar{Z}_s \cdot \bar{J}_n(k_{\rho 2} a_1)] \quad (6)$$

where

$$\bar{B}_n(k_{\rho 2} a_1) = \frac{1}{k_{\rho 2}^2 a_1} \begin{bmatrix} -j\omega\epsilon_2 k_{\rho 2} a_1 B'_n(k_{\rho 2} a_1) & -nk_z B_n(k_{\rho 2} a_1) \\ -nk_z B_n(k_{\rho 2} a_1) & j\omega\mu_2 k_{\rho 2} a_1 B'_n(k_{\rho 2} a_1) \end{bmatrix} \quad (7)$$

In the above and subsequently, $B_n(x)$ denotes either $J_n(x)$ or $H_n^{(2)}(x)$ corresponding to the $\bar{J}_n(x)$ or $\bar{H}_n^{(2)}(x)$ matrices, respectively. The special case of a perfectly conducting cylinder may be taken for which $Z_s = 0$ in (6).

In such a case, \bar{R}_{21} can be evaluated to be:

$$\bar{R}_{21} = \begin{bmatrix} -J_n(k_{\rho 2} a_1)/H_n^{(2)}(k_{\rho 2} a_1) & 0 \\ 0 & -J'_n(k_{\rho 2} a_1)/H_n^{(2)'}(k_{\rho 2} a_1) \end{bmatrix} \quad (8)$$

that corresponds to the reflection coefficients $-J_n(k_{\rho 2} a_1)/H_n^{(2)}(k_{\rho 2} a_1)$ and $-J'_n(k_{\rho 2} a_1)/H_n^{(2)'}(k_{\rho 2} a_1)$ for the TM and TE polarized waves, respectively that are decoupled from each other [23].

For the configuration in Fig. 1, the field radiated in Region 3 is given by:

$$\begin{bmatrix} E_{z3} \\ H_{z3} \end{bmatrix} = \frac{1}{2\pi} \int_{-\infty}^{\infty} dk_z e^{-jk_z(z-z')} \sum_{n=-\infty}^{\infty} e^{-jn(\theta-\phi')} \begin{bmatrix} \tilde{E}_{z3} \\ \tilde{H}_{z3} \end{bmatrix} \quad (9)$$

with the spectral components \tilde{E}_{z3} and \tilde{H}_{z3} being

$$\begin{bmatrix} \tilde{E}_{z3} \\ \tilde{H}_{z3} \end{bmatrix} = H_n^{(2)}(k_{\rho 3} \rho) \cdot \bar{T}_{23} \cdot (\bar{I} - \bar{R}_{21} \cdot \bar{R}_{23})^{-1} \cdot [J_n(k_{\rho 2} \rho') \cdot \bar{I} + H_n^{(2)}(k_{\rho 2} \rho') \cdot \bar{R}_{21}] \cdot \bar{D}' \quad (10)$$

In (10),

$$\bar{T}_{23} = \frac{2\omega}{\pi k_{\rho 2}^2 a_2} \cdot \bar{D}_{23}^{-1} \cdot \begin{bmatrix} \varepsilon_2 & 0 \\ 0 & -\mu_2 \end{bmatrix} \quad (11)$$

$$\bar{D}_{23} = \bar{J}_n(k_{\rho 2} a_2) \cdot H_n^{(2)}(k_{\rho 3} a_2) - \bar{H}_n^{(2)}(k_{\rho 3} a_2) \cdot J_n(k_{\rho 2} a_2) \quad (12)$$

$$\bar{R}_{23} = \bar{D}_{23}^{-1} \cdot [H_n^{(2)}(k_{\rho 2} a_2) \cdot \bar{H}_n^{(2)}(k_{\rho 3} a_2) - H_n^{(2)}(k_{\rho 3} a_2) \cdot \bar{H}_n^{(2)}(k_{\rho 2} a_2)] \quad (13)$$

$$\bar{B}_n(k_{\rho i} a_2) = \frac{1}{k_{\rho i}^2 a_2} \begin{bmatrix} -j\omega \varepsilon_i k_{\rho i} a_2 B'_n(k_{\rho i} a_2) & -nk_z B_n(k_{\rho i} a_2) \\ -nk_z B_n(k_{\rho i} a_2) & j\omega \mu_i k_{\rho i} a_2 B'_n(k_{\rho i} a_2) \end{bmatrix} \quad (14)$$

$$k_{\rho i}^2 = k_i^2 - k_z^2, \quad (i = 2, 3) \quad (15)$$

with the term \bar{T}_{23} denoting the 2×2 transmission matrix characterizing the wave transmission from Region 2 to Region 3.

3. Evaluation of space-wave

The space-wave radiation in the stratified cylindrical media originates from branch cuts associated with the branch points $k_z = \pm k_3$ in the outermost Region 3. For the branch cut $\text{Im}(k_{\rho 3}) = 0$, poles in the upper Riemann sheet corresponding to $\text{Im}(k_{\rho 3}) < 0$ satisfy the radiation condition at infinity while those in the lower Riemann sheet with $\text{Im}(k_{\rho 3}) > 0$ do not. In order to remove the branch point singularity in the complex k_z -plane, the k_z -plane is transformed into the complex w -plane ($w = \xi + j\eta$) by the transformation $k_z = k_3 \cos w$, with the double sheeted k_z -plane mapped into periodic strips of width 2π from $-\pi/2 < \xi < 3\pi/2$ in the w -plane. Replacing the Hankel function of the second kind by its asymptotic form for large argument, the Sommerfeld integral in the complex k_z -plane in (9) can be transformed from an integral along the real axis to the integral over the path P in the w -plane [13]. Thereafter, closed-form expressions of the space-wave can be obtained by evaluation of the Sommerfeld integral along the SDP (steepest descent path) in the w -plane. The final closed-form integrals corresponding to the space-wave are evaluated as :

$$\int_{-\infty}^{\infty} dk_z e^{-jk_z z} H_n^{(2)}(k_{\rho 3} \rho) F(\theta, \phi) = -2je^{\frac{jn\pi}{2}} F(\theta, \phi) \frac{e^{-jkr}}{r} \quad (16)$$

$$\int_{-\infty}^{\infty} dk_z e^{-jk_z z} \frac{\partial}{\partial \rho} (H_n^{(2)}(k_{\rho 3} \rho)) F(\theta, \phi) = -2k_3 e^{\frac{jn\pi}{2}} F(\theta, \phi) \sin \theta \frac{e^{-jkr}}{r} \quad (17)$$

where most of the integral contribution comes from the saddle point at $w = \theta$, with $F(\theta, \phi)$ describing the elevation and azimuthal dependence of the fields in the kernel. The radiated E_θ and E_ϕ -components of the fields can be thereafter obtained as in [13].

It can be noted here that the conclusions regarding the

contribution to the relevant space-wave harmonics for the $\hat{\rho}$, $\hat{\phi}$ and \hat{z} -directed sources mentioned in the paragraph following eqn. (14) in [13] is not valid in the current case. Particularly, the contribution to the space-wave radiation in the current configuration have to be evaluated by summing up over higher-order azimuthal harmonics till convergence is achieved. Also, a much higher space-wave directivity is achieved for the current configuration relative to [13], as demonstrated in Section 6.

4. Evaluation of leaky-wave

The leaky-wave region is caused by non-spectral poles in the lower Riemann sheet corresponding to waves growing along the radial direction and decaying along the longitudinal direction. Poles in the k_z -plane corresponding to (9) can be obtained from the condition :

$$(\bar{I} - \bar{R}_{21} \cdot \bar{R}_{23}) = \begin{bmatrix} G_1 & 0 \\ 0 & G_2 \end{bmatrix} = 0 \quad (18)$$

with

$$G_1 = 1 + \frac{t_1 t_2 t_3}{t_4 (t_3 t_5 - t_6)} \quad \text{and} \quad G_2 = 1 + \frac{t_7 t_8 t_9}{t_4 (t_3 t_5 - t_6)} \quad (19)$$

and

$$t_1 = \left(\frac{j\varepsilon_2 \omega Z_s J'_n(k_{\rho 2} a_1)}{k_{\rho 2}} + J_n(k_{\rho 2} a_1) \right) \left(\frac{j\mu_2 \omega H_n^{(2)'}(k_{\rho 2} a_1)}{k_{\rho 2} Z_s} + H_n^{(2)}(k_{\rho 2} a_1) \right) \quad (20)$$

$$t_2 = \left(\frac{-j\varepsilon_3 \omega H_n^{(2)'}(k_{\rho 3} a_2) H_n^{(2)}(k_{\rho 2} a_2)}{k_{\rho 3}} + \frac{j\varepsilon_2 \omega H_n^{(2)'}(k_{\rho 2} a_2) H_n^{(2)}(k_{\rho 3} a_2)}{k_{\rho 2}} \right) \quad (21)$$

$$t_3 = \left(\frac{-j\mu_3 \omega H_n^{(2)'}(k_{\rho 3} a_2) J_n(k_{\rho 2} a_2)}{k_{\rho 3}} + \frac{j\mu_2 \omega J'_n(k_{\rho 2} a_2) H_n^{(2)}(k_{\rho 3} a_2)}{k_{\rho 2}} \right) \quad (22)$$

$$t_4 = \left(\frac{-\varepsilon_2 \mu_2 \omega^2 H_n^{(2)'}(k_{\rho 2} a_1)^2}{k_{\rho 2}^2} + \frac{j\mu_2 \omega H_n^{(2)'}(k_{\rho 2} a_1) H_n^{(2)}(k_{\rho 2} a_1)}{Z_s k_{\rho 2}} + \frac{j\varepsilon_2 \omega Z_s H_n^{(2)'}(k_{\rho 2} a_1) H_n^{(2)}(k_{\rho 2} a_1)}{k_{\rho 2}} + H_n^{(2)}(k_{\rho 2} a_1)^2 \right) \quad (23)$$

$$t_5 = \left(\frac{j\varepsilon_3 \omega H_n^{(2)'}(k_{\rho 3} a_2) J_n(k_{\rho 2} a_2)}{k_{\rho 3}} - \frac{j\varepsilon_2 \omega J'_n(k_{\rho 2} a_2) H_n^{(2)}(k_{\rho 3} a_2)}{k_{\rho 2}} \right) \quad (24)$$

$$t_6 = \left(\frac{-nk_z J_n(k_{\rho 2} a_2) H_n^{(2)}(k_{\rho 3} a_2)}{a_2 k_{\rho 2}^2} + \frac{nk_z J_n(k_{\rho 2} a_2) H_n^{(2)}(k_{\rho 3} a_2)}{a_2 k_{\rho 3}^2} \right)^2 \quad (25)$$

$$t_7 = \left(\frac{j\mu_2 \omega Z_s J'_n(k_{\rho 2} a_1)}{k_{\rho 2} Z_s} + J_n(k_{\rho 2} a_1) \right) \left(\frac{j\varepsilon_2 \omega Z_s H_n^{(2)'}(k_{\rho 2} a_1)}{k_{\rho 2}} + H_n^{(2)}(k_{\rho 2} a_1) \right) \quad (26)$$

$$t_8 = \left(\frac{j\varepsilon_3 \omega H_n^{(2)'}(k_{\rho 3} a_2) J_n(k_{\rho 2} a_2)}{k_{\rho 3}} - \frac{j\varepsilon_2 \omega J'_n(k_{\rho 2} a_2) H_n^{(2)}(k_{\rho 3} a_2)}{k_{\rho 2}} \right) \quad (27)$$

$$t_9 = \left(\frac{j\mu_3 \omega H_n^{(2)'}(k_{\rho 3} a_2) H_n^{(2)}(k_{\rho 2} a_2)}{k_{\rho 3}} - \frac{j\mu_2 \omega H_n^{(2)'}(k_{\rho 2} a_2) H_n^{(2)}(k_{\rho 3} a_2)}{k_{\rho 2}} \right) \quad (28)$$

Maximum contribution of a leaky-wave pole in the radiation pattern will occur corresponding to minimum imaginary part of k_z for a discrete n . It can be also noted here that the leaky-wave mechanism is fundamentally different in the current configuration relative to [13] since the dominant leaky-wave poles corresponding to low attenuation constant are contributed by the term $(\bar{I} - \bar{R}_{21} \cdot \bar{R}_{23})$ characterizing the local reflections at the dielectric-to-impedance surface and the dielectric-to-air interfaces, instead of the poles of the

transmission matrix \bar{T}_{23} corresponding to \bar{D}_{23} in (12). This can be compared to [13], where the dominant leaky-wave poles are contributed by the poles of the transmission matrix \bar{T}_{12} . As a result, the leaky-wave directivity is found to be much higher in the current antenna configuration relative to [13] or that achieved using a single impedance surface.

It can also be noted that the contribution to the leaky-wave radiation from a \hat{z} - or $\hat{\rho}$ - polarized source comes from the term G_1 while the term G_2 contributes to the leaky-wave radiation for a $\hat{\phi}$ - directed source. The integral in (9) corresponding to leaky-wave radiation can be evaluated using (16) and (17), with the summation over n in the term $F(\theta, \phi)$ restricted to the dominant term. However, as compared to [13] where $n=0$ corresponded to the dominant contribution to the leaky-mode radiation, it is observed that for the current configuration, the contribution to the dominant leaky-mode radiation arises from higher values of n as demonstrated subsequently.

The leaky-wave radiation pattern for \hat{z} / $\hat{\rho}$ - directed sources can be obtained as :

$$E_\theta = \frac{1}{\pi} e^{jn\frac{\pi}{2}} e^{-jn(\phi-\phi')} e^{jk_z z'} \frac{jk_3}{k_{\rho 3}} E'_\theta \frac{1}{G_1} \frac{e^{-jk_3 r}}{r} \quad (29)$$

with the leaky-wave pattern for the $\hat{\phi}$ - directed source given by :

$$E_\phi = -\frac{1}{\pi} e^{jn\frac{\pi}{2}} e^{-jn(\phi-\phi')} e^{jk_z z'} \frac{j\mu_3}{k_{\rho 3}} E'_\phi \frac{1}{G_2} \frac{e^{-jk_3 r}}{r} \quad (30)$$

with

$$\begin{bmatrix} E'_\theta \\ E'_\phi \end{bmatrix} = \bar{T}_{23} \cdot [J_n(k_{\rho 2} \rho') \cdot \bar{I} + H_n^{(2)}(k_{\rho 2} \rho') \cdot \bar{R}_{21}] \cdot \bar{D}'_2 \quad (31)$$

Finally, the $1/G_i$ term for $i=1,2$ can be expressed in terms of the pole k_{pz} as in (22) of [13].

5. Evaluation of creeping-wave

Creeping-wave corresponds to the wave that flow along the surface of the cylinder and is responsible for wave radiation in shadow region. They are characterized by the term $f_i(v) = \frac{N(v)}{D(v)}$ [13], [24] with the azimuthal summation

replaced by the summation over the residues corresponding to the poles using Watson's transformation. The creeping-wave poles for the current configuration are obtained from $G_1=0$ for \hat{z} - or $\hat{\rho}$ -directed source and $G_2=0$ for $\hat{\phi}$ -directed source from (19) for $n=v(=v'-jv'')$, v' and v'' being the azimuthal propagation and attenuation constants, respectively for the creeping-wave. As a result, the creeping-wave poles depend on the source polarization. This can be compared with [13] where the creeping-wave poles are independent of the source polarization. The term $N(v)$ for the current configuration is evaluated as :

For \hat{z} - or $\hat{\rho}$ - directed source

$$N(v) = \frac{1}{\pi} e^{jv\frac{\pi}{2}} e^{jv\phi'} e^{jk_z z'} \frac{jk_3}{k_{\rho 3}} E'_\theta \quad (32)$$

and for $\hat{\phi}$ - directed source

$$N(v) = -\frac{1}{\pi} e^{jv\frac{\pi}{2}} e^{jv\phi'} e^{jk_z z'} \frac{j\mu_3}{k_{\rho 3}} E'_\phi \quad (33)$$

where E'_θ and E'_ϕ in (32) and (33) respectively can be obtained from (31) for $n=v$.

6. Results and discussion

6.1. Space-wave radiation

In this section, the space-wave radiation characteristics for the dielectric-coated impedance cylinder are examined for different source polarizations with the source located at the center of the dielectric coating at $\rho' = (a_1 + a_2)/2$ for this and all subsequent cases discussed in the paper. The variation in the space-wave radiation characteristics with the coated impedance cylinder parameters is shown in Fig. 2, for excitation with a \hat{z} - directed source, with the outer medium (Region 3) as free space. Fig. 2(a) shows the pattern characteristics with variation in the permittivity of the dielectric coating for the inner and outer layer radii $a_1 = 0.47\lambda_0$, $a_2 = 0.74\lambda_0$ and $Z_s = (1+j)\Omega$. A maximum directivity of 28.94 dB is obtained for $\epsilon_{r2} = 11.9$ with beam directions at 38.59° and 141.41° . It is observed that convergence in the space-wave radiation characteristics is obtained within the range of $n = -20$ - 20 for this and the subsequent space-wave patterns. The results for this case are also compared with simulation. The simulations throughout the paper have been conducted using the High-Frequency Structure Simulator [25], with a \hat{z} -directed electric source of dimension $\lambda_0/50$ and the length of the coated cylinder as $12\lambda_0$. An excellent agreement between the theoretical and simulated results is observed. The space-wave directivity obtained for the dielectric coated impedance cylinder structure is also observed to be much higher than that obtained for the cylindrical rod structure in [13]. This was also verified to be true for comparable parameters and dimensions of the current antenna structure and the cylindrical rod antenna in [13] for this and the following cases of space-wave radiation described below.

The variation in the space-wave characteristics with the radius of the impedance surface a_1 for $\epsilon_{r2} = 3.9$, $Z_s = (1+j)\Omega$ is next investigated with the coating thickness maintained at $0.27\lambda_0$ as in Fig. 2(a) (Fig. 2(b)). It is observed that for $a_1 = 0.46\lambda_0$, a maximum directivity of 25.97 dB is achieved with the beam directions at 47.74° and 132.26° . The beam is also seen to gradually scan towards the cylinder axis for $0.45\lambda_0 \leq a_1 \leq 0.48\lambda_0$. The directivity is however reduced to about 13.52 dB for $a_1 = 0.48\lambda_0$ due to an increase in the side lobe level.

The space-wave characteristics with the variation in the outer dielectric radius a_2 is shown in Fig. 2(c). A maximum directivity of 23.75 dB is observed at $a_2 = 0.74\lambda_0$, at beam directions of 45.07° and 134.93° , with the beam gradually scanning towards the cylinder axis with increase in the outer dielectric radius. However, compared with Fig. 2(b), an increase in the outer dielectric radius has a lesser effect on the directivity reduction due to a gradual

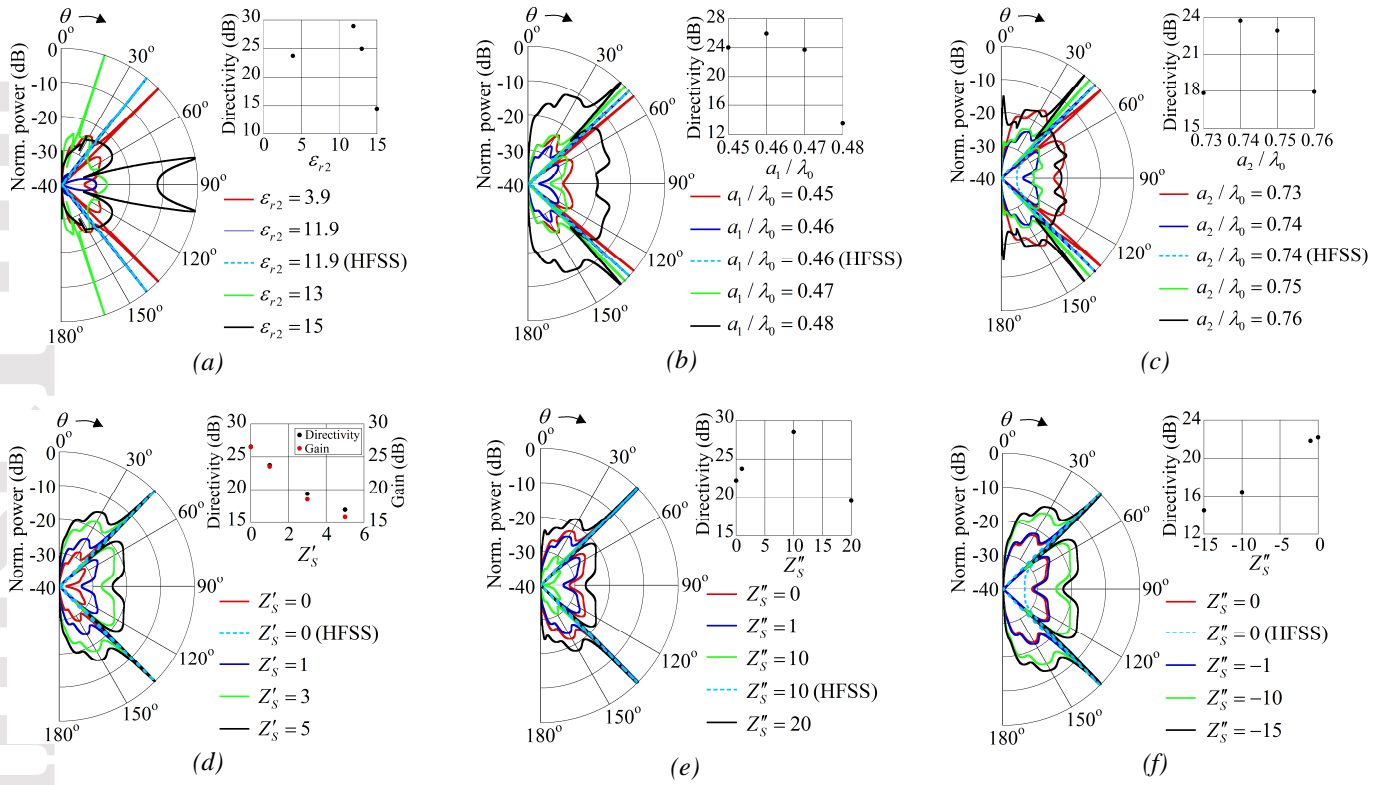


Fig. 2. Variation of space-wave radiation pattern for excitation with a \hat{z} -directed source with (a) ϵ_{r2} : $a_1 = 0.47\lambda_0$, $a_2 = 0.74\lambda_0$, $Z_s = (1+j)\Omega$, (b) a_1/λ_0 : $\epsilon_{r2} = 3.9$, $a_2 - a_1 = 0.27\lambda_0$, $Z_s = (1+j)\Omega$, (c) a_2/λ_0 : $\epsilon_{r2} = 3.9$, $a_1 = 0.47\lambda_0$, $Z_s = (1+j)\Omega$, (d) $Z'_s(\Omega)$: $\epsilon_{r2} = 3.9$, $a_1 = 0.47\lambda_0$, $a_2 = 0.74\lambda_0$, $Z''_s = 1\Omega$, (e) $Z''_s(\Omega)$: $\epsilon_{r2} = 3.9$, $a_1 = 0.47\lambda_0$, $a_2 = 0.74\lambda_0$, $Z'_s = 1\Omega$ and (f) $Z''_s(\Omega)$: $\epsilon_{r2} = 3.9$, $a_1 = 0.47\lambda_0$, $a_2 = 0.74\lambda_0$, $Z'_s = 1\Omega$.

enhancement in the side-lobe level in this case.

The effect of an increase in the real part of the surface impedance on the radiation characteristics is next investigated (Fig. 2(d)). It is observed that the beam-direction is almost unaffected with increasing Z'_s . A maximum directivity of 26.56 dB is obtained at the beam-directions of 45.07° and 134.93° for $Z'_s = 0\Omega$. Thereafter, an increase in Z'_s causes an increase in the side-lobe level resulting in a reduction in directivity. The simulated gain obtained through HFSS is also shown in this case due to the loss of the inner core. It can be observed that the reduction in gain with increase in Z'_s is minimal, with the maximum gain reduction around 1.1 dB at $Z'_s = 5\Omega$.

Next, the space-wave characteristics with variation in the imaginary part of the surface impedance Z''_s is investigated. The variation in the space-wave characteristics for positive values of Z''_s is shown in Fig. 2(e) while Fig. 2(f) shows the space-wave variation for negative values of Z''_s . It can be observed from Fig. 2(e) that an optimum value of directivity of 28.54 dB is obtained for $Z''_s = 10\Omega$ with beam directions at 44.78° and 135.22° . For increasing or decreasing Z''_s beyond the optimum value of $Z''_s = 10\Omega$, the directivity is reduced due to an enhancement in the side-lobe level. This can be compared with Fig. 2(f) where a steady reduction in directivity is observed as Z''_s reduces below 0, with a maximum directivity of 22.21 dB at $Z''_s = 0\Omega$. It is also seen from Figs. 2(e) and (f) that the

beam-direction is almost independent with positive or negative excursions of Z''_s .

The space-wave characteristics excited with a $\hat{\rho}$ -directed source for the structure is next investigated. Fig. 3(a) shows the variation in space-wave radiation with change in the permittivity of the dielectric coating. It can be observed that a maximum directivity of 27.95 dB is obtained for $\epsilon_{r2} = 13$ with beam directions at 18.29° and 161.71° . Though not shown in the figure, the directivity sharply reduces for $\epsilon_{r2} > 13$ due to an increase in the side-lobe level. The results for the optimum case are also verified with simulations, using a $\hat{\rho}$ -directed source of length $\lambda_0/50$.

The effect of the variation in the radius of the impedance surface a_1 on the space-wave radiation is next examined for the $\hat{\rho}$ -directed source (Fig. 3(b)). It is observed that a maximum directivity of 28.54 dB is obtained at $a_1 = 0.46\lambda_0$ that is higher than the corresponding directivity obtained in Fig. 2(b) with the \hat{z} -directed source. A similar characteristic is observed in Fig. 3(c), with a maximum directivity of 27.20 dB at $a_2 = 0.74\lambda_0$ that is higher than the pattern directivity in Fig. 2(c). The space-wave variation with Z'_s and Z''_s shown in Figs. 3(d) – (f) also shows that the optimum directivity achieved by excitation with the $\hat{\rho}$ -directed source are at 29.22 dB, 31.21 dB and 26.02 dB respectively, which are higher than the directivity values obtained in Figs. 2(d) – (f) corresponding to the excitation using the \hat{z} -directed source. The simulated

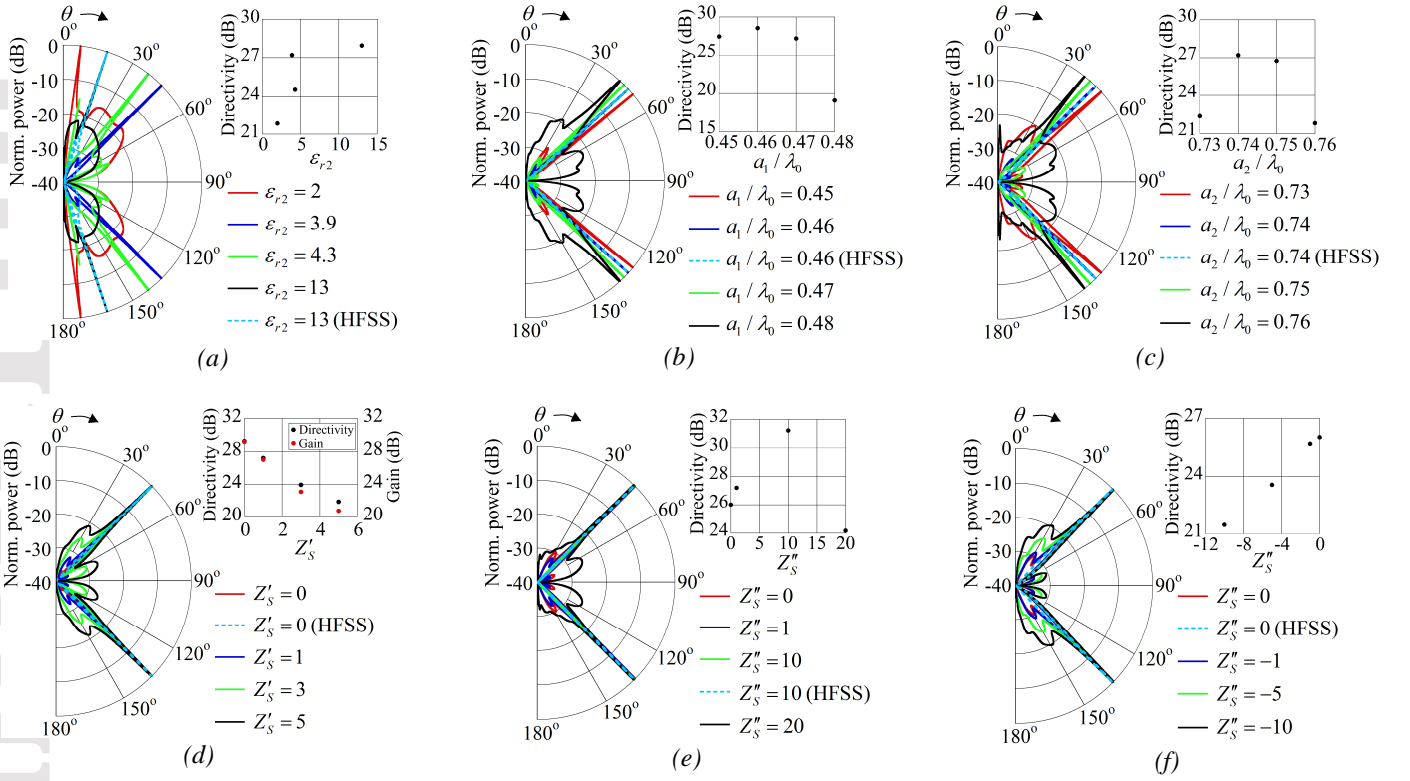


Fig. 3. Variation of space-wave radiation pattern for excitation with a \hat{p} -directed source with (a) ϵ_{r2} : $a_1 = 0.47\lambda_0$, $a_2 = 0.74\lambda_0$, $Z_s = (1 + j)\Omega$, (b) a_1/λ_0 : $\epsilon_{r2} = 3.9$, $a_2 - a_1 = 0.27\lambda_0$, $Z_s = (1 + j)\Omega$, (c) a_2/λ_0 : $\epsilon_{r2} = 3.9$, $a_1 = 0.47\lambda_0$, $Z_s = (1 + j)\Omega$, (d) $Z'_s(\Omega)$: $\epsilon_{r2} = 3.9$, $a_1 = 0.47\lambda_0$, $a_2 = 0.74\lambda_0$, $Z'_s = 1\Omega$, (e) $Z''_s(\Omega)$: $\epsilon_{r2} = 3.9$, $a_1 = 0.47\lambda_0$, $a_2 = 0.74\lambda_0$, $Z'_s = 1\Omega$ and (f) $Z''_s(\Omega)$: $\epsilon_{r2} = 3.9$, $a_1 = 0.47\lambda_0$, $a_2 = 0.74\lambda_0$, $Z'_s = 1\Omega$.

gain characteristics in Fig. 3(d) also show that a minimal gain reduction is obtained at around 1.1 dB at $Z'_s = 5\Omega$.

For the $\hat{\phi}$ -directed source, it is however observed that the space-wave directivity is lower compared to that corresponding to the \hat{z} - and \hat{p} -directed sources. As such, this case is not discussed for brevity.

It can be noted that by looking into the air-dielectric boundary at $\rho = a_2$, one might find the equivalent impedance which accounts for the impedance cylinder plus the dielectric layer of Region 2. However, the thick dielectric coating of $0.27\lambda_0$ as in the current work have to be modeled, taking into account the impedance surface and the TE-TM coupling in the dielectric layer, which would be complex. In addition, we would not be able to analyze the present configuration with the source inside the dielectric layer. It is also found that the pattern directivity with the source inside the dielectric is higher compared to the cases where the source is on the outside surface or in the air region (Region 3).

6.2. Leaky-wave radiation

The leaky-wave radiation, caused due to non-spectral poles in the lower Riemann sheet are characterized by $G_1 = 0$ and $G_2 = 0$ for \hat{z}/\hat{p} - and $\hat{\phi}$ -directed sources, respectively. It might be noted that the dominant contribution to the leaky-wave radiation for discrete n is contributed by poles in the k_z -plane with minimum

imaginary part k_z'' , satisfying the fast-wave condition $k_z'/k_0 < 1$. The variation in the normalized leaky-wave phase and attenuation constants k_z'/k_0 and k_z''/k_0 respectively with respect to the design parameters are shown in Fig. 4 for excitation with the \hat{z}/\hat{p} -directed source. The variation of the complex propagation constant with change in the permittivity of the dielectric coating is shown in Fig. 4(a). For Fig. 4(a), only dominant poles corresponding to lowest k_z''/k_0 values for discrete $n = 3, 5$ and 9 are shown for clarity. In this and the following, the values of n that are not considered correspond to either the non-existence of leaky-wave poles or k_z''/k_0 being high corresponding to a leaky-wave pole, corresponding to low-directivity. However, it must be noted that, some poles in Fig. 4(a) e.g. for $\epsilon_{r2} = 27, 28$ and 29 that are just outside the fast-wave condition correspond to proper surface-waves in the upper Riemann sheet. It can also be observed that in the region $\epsilon_{r2} = 19 - 22$, no leaky-wave poles are present. The current configuration can be compared with [13], where the dominant leaky-mode pole always corresponds to $n = 0$ compared to the higher-order azimuthal harmonics contributing to the leaky-wave mechanism in this case.

The leaky-wave radiation characteristics with variation in permittivity of the dielectric coating for excitation with the \hat{z}/\hat{p} -directed source is shown in Fig. 6(a). In plotting the patterns, $n = 5$ is chosen for $\epsilon_{r2} = 3.9$ and 11.9 , $n = 9$ for $\epsilon_{r2} = 9$ and 15 while for $\epsilon_{r2} = 13$,

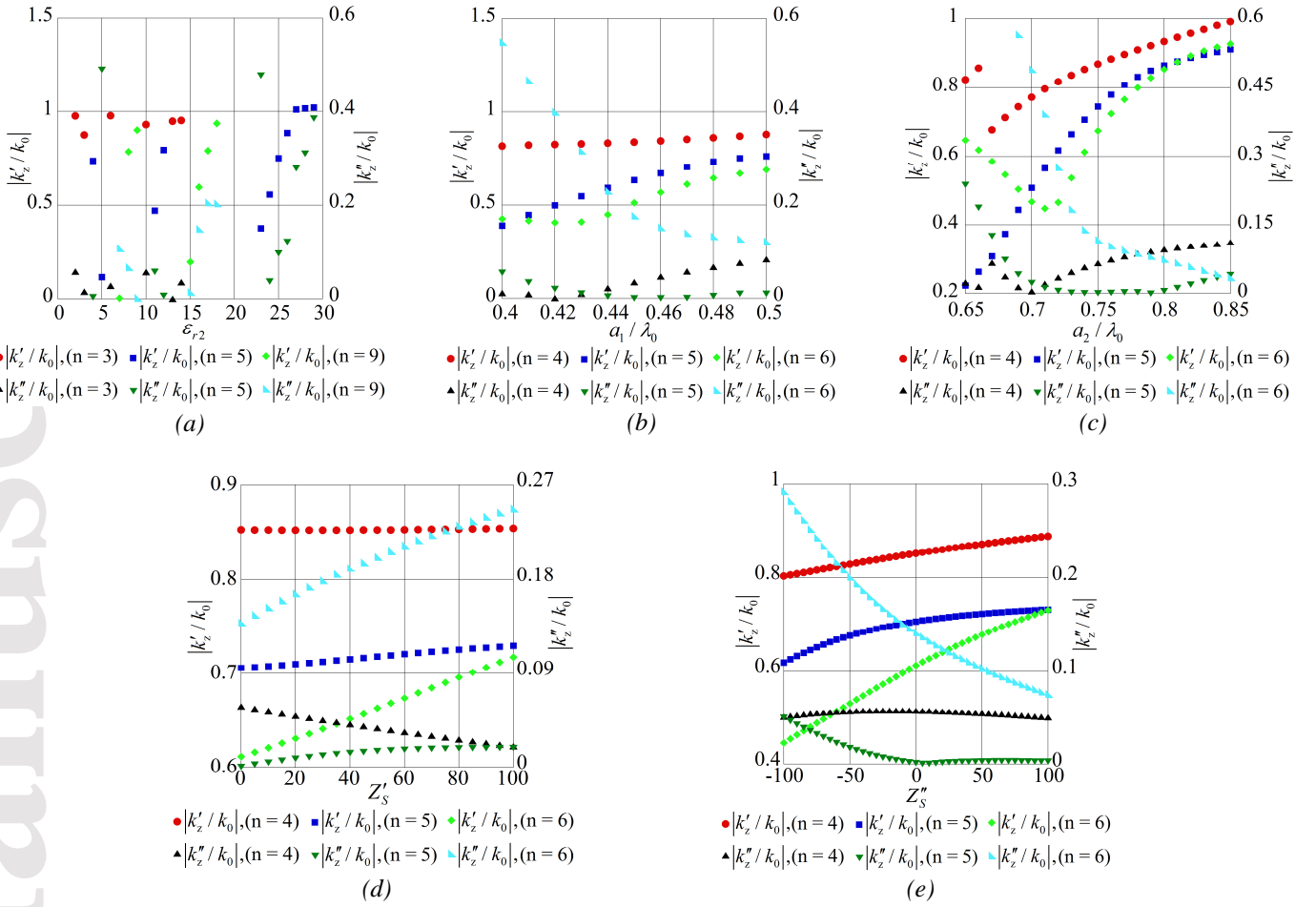


Fig. 4. Variation of the normalized leaky-wave phase and attenuation constants for excitation with a \hat{z} - or $\hat{\rho}$ -directed source with (a) ϵ_{r2} : $a_1 = 0.47\lambda_0$, $a_2 = 0.74\lambda_0$, $Z_s = (1+j)\Omega$, (b) a_1/λ_0 : $\epsilon_{r2} = 3.9$, $a_2 - a_1 = 0.27\lambda_0$, $Z_s = (1+j)\Omega$ (c) a_2/λ_0 : $\epsilon_{r2} = 3.9$, $a_1 = 0.47\lambda_0$, $Z_s = (1+j)\Omega$ (d) $Z'_s (\Omega)$: $\epsilon_{r2} = 3.9$, $a_1 = 0.47\lambda_0$, $a_2 = 0.74\lambda_0$, $Z''_s = 1\Omega$ and (e) $Z''_s (\Omega)$: $a_1 = 0.47\lambda_0$, $a_2 = 0.74\lambda_0$, $Z'_s = 1\Omega$.

$n=3$ are chosen, corresponding to the minimum values of k''_z/k_0 . It is observed that for the case of $\epsilon_{r2} = 9$, the directivity is comparatively lower than for the other cases due to an enhanced radiation around $\theta=90^\circ$, in spite of a small beamwidth at $\theta=26.33^\circ$ and 153.67° in the directions of maximum radiation. A maximum directivity of 31.20 dB is obtained for a coating permittivity of $\epsilon_{r2} = 13$ with $\hat{z}/\hat{\rho}$ -directed source excitation. The directivity is also observed to be much higher than that obtained in Fig. 6(a) [13] for the leaky-wave.

The variation of the leaky-wave propagation constant with variation in the radius of the impedance surface is shown in Fig. 4(b) for $n=4, 5$ and 6. It is observed that corresponding to the above values of n , leaky-waves are supported in the range $0.4 \leq a_1/\lambda_0 \leq 0.5$. It is seen from Fig. 4(b) that the attenuation constant corresponding to $n=5$ is the lowest in the range $0.44 \leq a_1/\lambda_0 \leq 0.5$, with minimum value at $a_1 = 0.46\lambda_0$. The radiation characteristics in the range $0.45 \leq a_1/\lambda_0 \leq 0.475$ is shown in Fig. 6(b) for $n=5$. A maximum directivity of 27.38 dB is observed for $a_1 = 0.46\lambda_0$.

Fig. 4(c) shows the leaky-wave propagation

characteristics with variation in the radius of the dielectric coating. It is observed from the attenuation characteristics in Fig. 4(c) that an effective leaky-wave operating region can be obtained from $0.72 \leq a_2/\lambda_0 \leq 0.8$ for $n=5$ corresponding to the lowest values of k''_z/k_0 . A discontinuity in the phase constant is observed at $a_2/\lambda_0 = 0.66$ for $n=4$ corresponding to the transition of the leaky-wave pole to the guided mode region ($k'_z/k_0 > 1$) and back to the leaky-wave wave propagation region. The radiation characteristics in the range $0.73 \leq a_2/\lambda_0 \leq 0.755$ is shown in Fig. 6(c). A maximum directivity of 25.90 dB at $a_2 = 0.74\lambda_0$ is obtained.

The variation in the leaky-wave propagation constant with the real part of the surface impedance is shown in Fig. 4(d). A fast-wave region is obtained for $0 \leq Z'_s \leq 100 \Omega$ with the lowest attenuation obtained for $Z'_s = 0 \Omega$, $n=5$. The corresponding radiation characteristics in Fig. 6(d) show a steady reduction in directivity with increasing Z'_s from the maximum directivity value of 27.83 dB, with the beam direction almost invariant with change in Z'_s . The simulated gain in this case show a maximum gain reduction of about 5.1 dB at $Z'_s = 5 \Omega$.

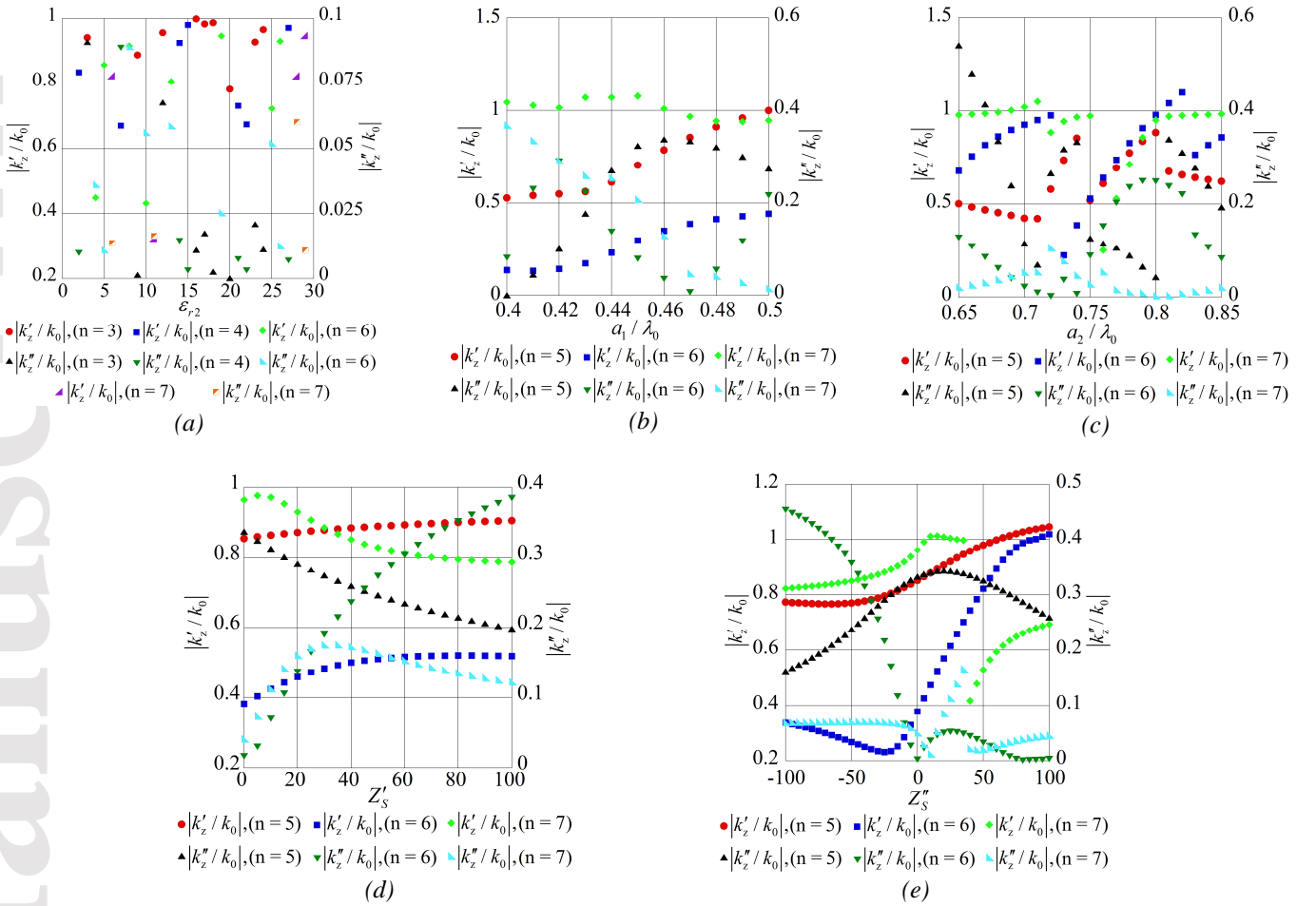


Fig. 5. Variation of the normalized leaky-wave phase and attenuation constants for excitation with a $\hat{\phi}$ -directed source with (a) ϵ_{r2} : $a_1 = 0.47\lambda_0$, $a_2 = 0.74\lambda_0$, $Z_s = (1 + j)\Omega$, (b) a_1/λ_0 : $\epsilon_{r2} = 9.8$, $a_2 - a_1 = 0.27\lambda_0$, $Z_s = (1 + j)\Omega$, (c) a_2/λ_0 : $\epsilon_{r2} = 9.8$, $a_1 = 0.47\lambda_0$, $Z_s = (1 + j)\Omega$, (d) $Z'_s (\Omega)$: $\epsilon_{r2} = 9.8$, $a_1 = 0.47\lambda_0$, $a_2 = 0.74\lambda_0$, $Z''_s = 1\Omega$ and (e) $Z''_s (\Omega)$: $a_1 = 0.47\lambda_0$, $a_2 = 0.74\lambda_0$, $Z'_s = 1\Omega$.

Fig. 4(e) shows the leaky-wave propagation characteristics with change in the imaginary part of the surface impedance. It is observed that the lowest attenuation characteristics are obtained for $n=5$ for $Z''_s > 0\Omega$ compared to negative values of Z''_s . The minimum attenuation occurs at $Z''_s = 10\Omega$, $n=5$ corresponding to which the highest directivity of 29.84 dB is obtained in Fig. 6(e), with a steady reduction in directivity with decrease in Z''_s in Fig. 6(f) corresponding to a gradual increase in attenuation with reduction in Z''_s for $Z''_s < 0\Omega$ in Fig. 4(e). It can also be noted that as for the space-wave, the leaky-wave directivity is significantly higher for the current dielectric coated impedance cylinder compared to the cylindrical rod antenna in [13] for comparable parameters and dimensions of both antenna structures for all cases of leaky-wave radiation.

The leaky-wave characteristics for excitation with a $\hat{\phi}$ -directed source is next investigated (Fig. 5). Fig. 5(a) shows the leaky-wave propagation constant with change in the coating permittivity, where only the dominant leaky-wave pole with the lowest values of attenuation constant for a given permittivity is shown for $n=3, 4, 6$ and 7 . It can be

observed that for $\epsilon_{r2} = 15-18$, k'_z/k_0 is near to 1 corresponding to the proper surface-wave region. The leaky-wave radiation characteristics are shown in Fig. 7(a) for the values of the coating permittivities with the lowest attenuation constants which are at $\epsilon_{r2} = 9$, $\epsilon_{r2} = 9.8$, $\epsilon_{r2} = 20$ and $\epsilon_{r2} = 22$ with $n=3, 6, 3$ and 4 , respectively. The highest directivity of 27.83 dB is obtained for a coating permittivity of $\epsilon_{r2} = 20$, much higher than that obtained in [13].

The propagation characteristics of the leaky-wave with variation in the radius of the impedance surface for excitation with the $\hat{\phi}$ -directed source is shown in Fig. 5(b). For this and all subsequent cases of Fig. 5, the relevant values of n corresponding to leaky-wave poles are at $n=5, 6$ and 7 . It can however be seen from the variation of the real part of the propagation constant from Fig. 5(b) that the maximum leaky-wave operating range occurs for the $n=5$ and 6 harmonics, with the real part of the propagation constant in the vicinity of the upper Riemann sheet surface-wave region for $n=7$. The corresponding radiation characteristics are shown in Fig. 7(b) in the range $0.46 \leq a_1/\lambda_0 \leq 0.473$, with the dominant contribution due to

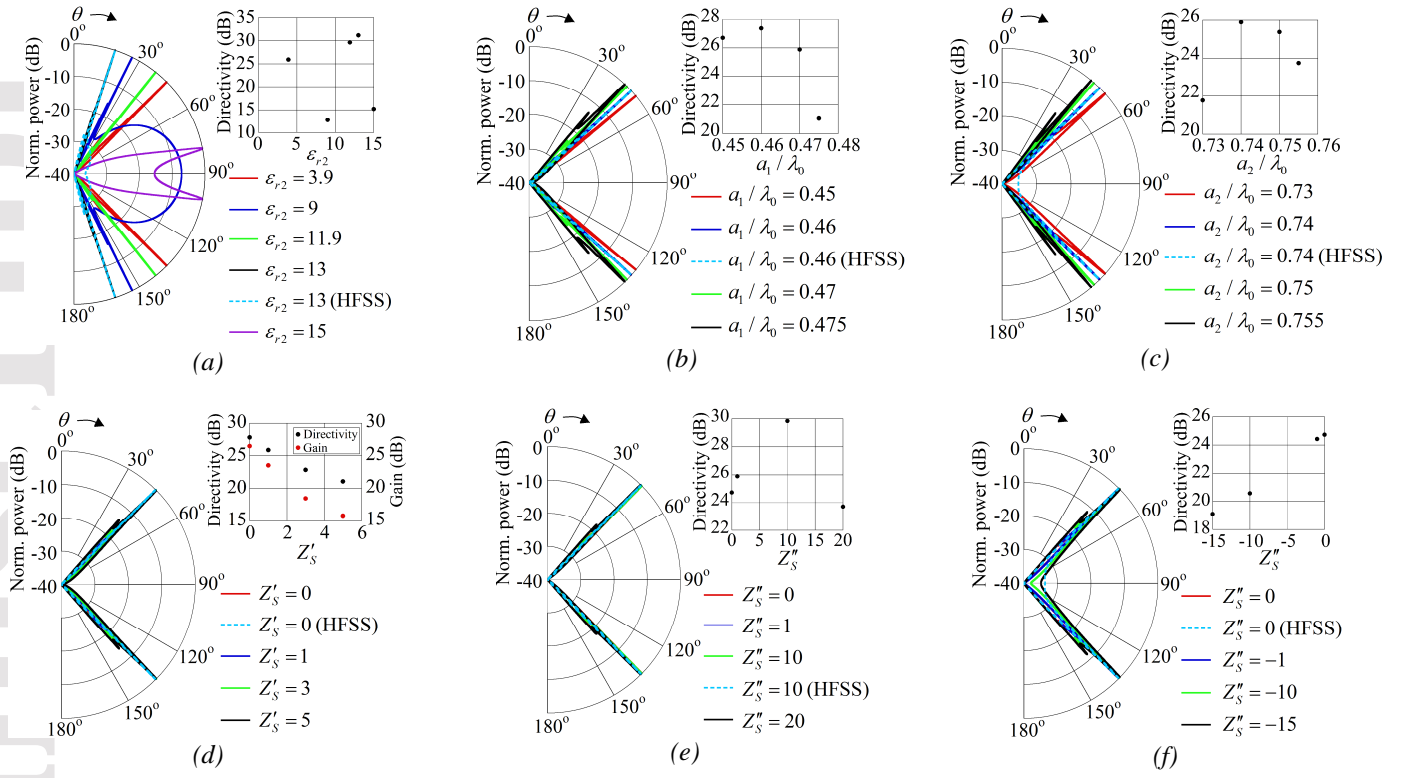


Fig. 6. Variation of leaky-wave radiation pattern for excitation with a \hat{z} - or \hat{p} -directed source with (a) ϵ_{r2} : $a_1 = 0.47\lambda_0$, $a_2 = 0.74\lambda_0$, $Z_S = (1+1j)\Omega$, (b) a_1/λ_0 : $\epsilon_{r2} = 3.9$, $a_2 - a_1 = 0.27\lambda_0$, $Z_S = (1+1j)\Omega$, (c) a_2/λ_0 : $\epsilon_{r2} = 3.9$, $a_1 = 0.47\lambda_0$, $Z_S = (1+1j)\Omega$, (d) $Z'_S(\Omega)$: $\epsilon_{r2} = 3.9$, $a_1 = 0.47\lambda_0$, $a_2 = 0.74\lambda_0$, $Z'_S = 1\Omega$, (e) $Z''_S(\Omega)$: $\epsilon_{r2} = 3.9$, $a_1 = 0.47\lambda_0$, $a_2 = 0.74\lambda_0$, $Z'_S = 1\Omega$ and (f) $Z''_S(\Omega)$: $\epsilon_{r2} = 3.9$, $a_1 = 0.47\lambda_0$, $a_2 = 0.74\lambda_0$, $Z'_S = 1\Omega$.

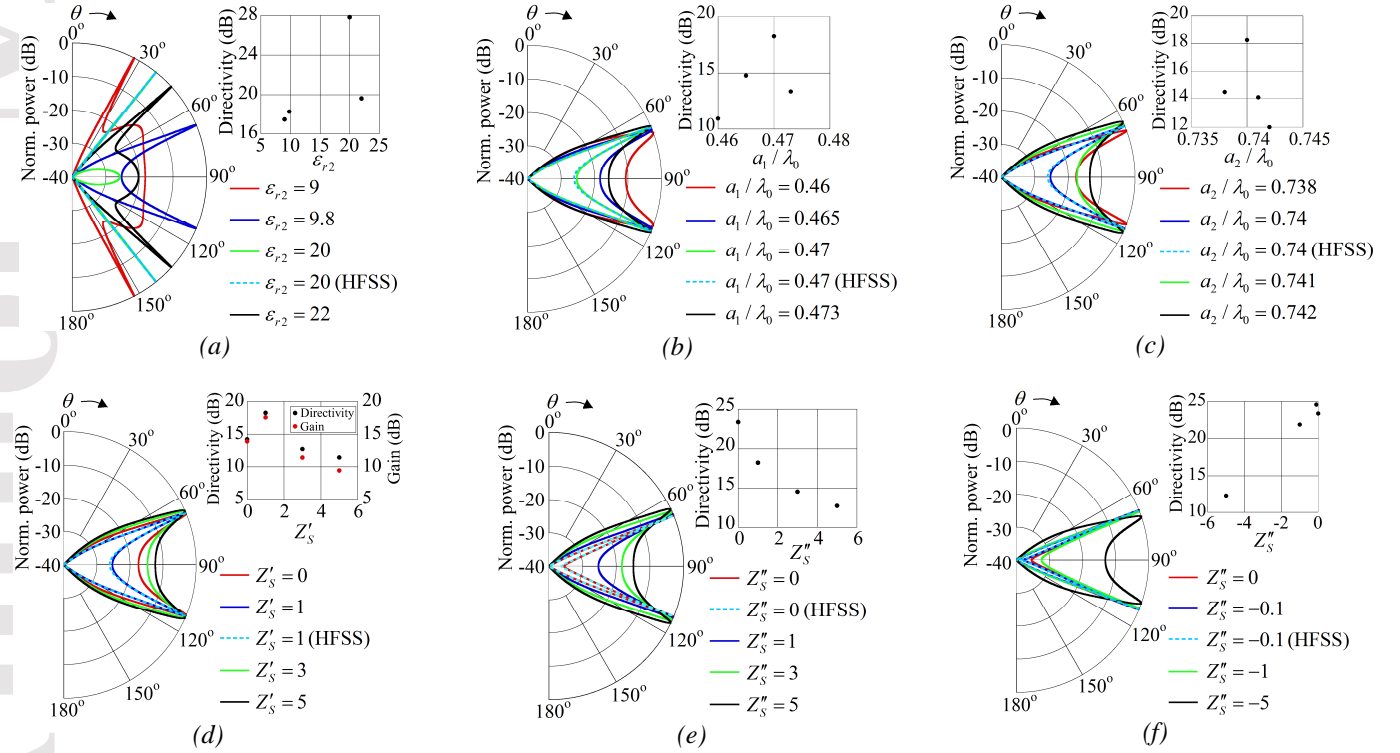


Fig. 7. Variation of leaky-wave radiation pattern for excitation with a $\hat{\phi}$ -directed source with (a) ϵ_{r2} : $a_1 = 0.47\lambda_0$, $a_2 = 0.74\lambda_0$, $Z_S = (1+1j)\Omega$, (b) a_1/λ_0 : $\epsilon_{r2} = 9.8$, $a_2 - a_1 = 0.27\lambda_0$, $Z_S = (1+1j)\Omega$, (c) a_2/λ_0 : $\epsilon_{r2} = 9.8$, $a_1 = 0.47\lambda_0$, $Z_S = (1+1j)\Omega$, (d) $Z'_S(\Omega)$: $\epsilon_{r2} = 9.8$, $a_1 = 0.47\lambda_0$, $a_2 = 0.74\lambda_0$, $Z'_S = 1\Omega$, (e) $Z''_S(\Omega)$: $\epsilon_{r2} = 9.8$, $a_1 = 0.47\lambda_0$, $a_2 = 0.74\lambda_0$, $Z'_S = 1\Omega$ and (f) $Z''_S(\Omega)$: $\epsilon_{r2} = 9.8$, $a_1 = 0.47\lambda_0$, $a_2 = 0.74\lambda_0$, $Z'_S = 1\Omega$.

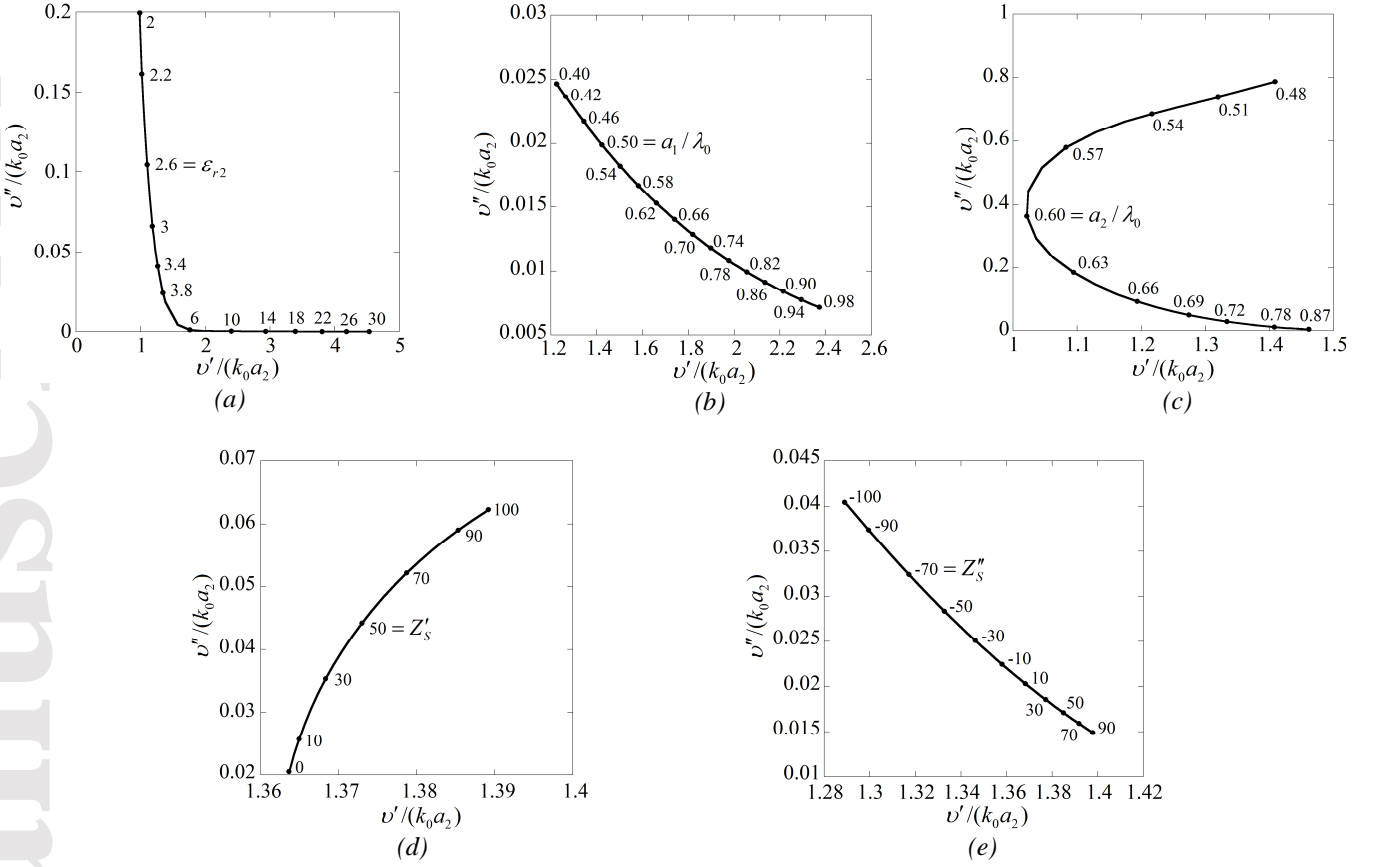


Fig. 8. Normalized creeping-wave pole loci in the complex v -plane for \hat{z} - or \hat{p} -directed electric source excitation with variation in (a) ϵ_{r2} : $a_1 = 0.47\lambda_0$, $a_2 = 0.74\lambda_0$, $Z_s = (1+j)\Omega$, (b) a_1/λ_0 : $\epsilon_{r2} = 3.9$, $a_2 - a_1 = 0.27\lambda_0$, $Z_s = (1+j)\Omega$, (c) a_2/λ_0 : $\epsilon_{r2} = 3.9$, $a_1 = 0.47\lambda_0$, $Z_s = (1+j)\Omega$, (d) $Z'_s(\Omega)$: $\epsilon_{r2} = 3.9$, $a_1 = 0.47\lambda_0$, $a_2 = 0.74\lambda_0$, $Z''_s = 1\Omega$ and (e) $Z''_s(\Omega)$: $\epsilon_{r2} = 3.9$, $a_1 = 0.47\lambda_0$, $a_2 = 0.74\lambda_0$, $Z'_s = 1\Omega$.

the $n=6$ harmonic. A maximum directivity of 18.27 dB is observed at $a_1 = 0.47\lambda_0$.

The leaky-wave propagation constant with variation in the radius of the dielectric coating is shown in Fig. 5(c). It is observed that the real part of the propagation constant for $n=5$ possess discontinuities at $a_2 = 0.74\lambda_0$ and $0.8\lambda_0$ for which the leaky-wave pole migrates to the proper surface-wave region and thereafter returns to the leaky-wave propagation region. A similar discontinuity is observed at $a_2 = 0.72\lambda_0$ and at $a_2 = 0.82\lambda_0$ for $n=6$ and at $a_2 = 0.71\lambda_0$ and at $a_2 = 0.75\lambda_0$ for $n=7$. The radiation characteristics in Fig. 7(c) are shown for $0.738 \leq a_2/\lambda_0 \leq 0.742$ corresponding to which the attenuation constant is minimum for the $n=6$ harmonic with the phase constant $k'_z/k_0 = 0.387$ at $a_2 = 0.74\lambda_0$ being well inside the leaky-wave region corresponding to radiation nearer to broadside. A maximum directivity of 18.27 dB is obtained at $a_2 = 0.74\lambda_0$.

The variation in the leaky-wave propagation constant with the real part of the surface impedance is shown in Fig. 5(d). It can be observed that upto $Z'_s = 25\Omega$, the dominant contribution to the leaky-wave with minimum attenuation constant is contributed by the $n=6$ harmonic, with $n=7$ being dominant thereafter. The radiation characteristics with change in the surface impedance is shown in Fig. 7(d). A

maximum directivity of 18.27 dB is noted for $Z'_s = 1\Omega$.

The simulated gain characteristics show a maximum gain reduction of about 2 dB at $Z'_s = 5\Omega$.

The leaky-wave propagation constant with variation in the imaginary part of the surface impedance is shown in Fig. 5(e). A minimum attenuation range is observed in the range $-10 < Z''_s < 5\Omega$ for the $n=6$ harmonic, with the phase constant deep within the leaky-wave region. The corresponding radiation characteristics are shown in Figs. 7(e) and (f) for $Z''_s > 0\Omega$ and $Z''_s < 0\Omega$ respectively. The maximum directivity of 24.59 dB is achieved at $Z''_s = -0.1\Omega$, with a steady reduction in directivity for $Z''_s > 0\Omega$ and $Z''_s < -0.1\Omega$.

It may be noted that the space-wave radiation in the antenna configuration generates from the branch cuts associated with the branch points $k_z = \pm k_3$ corresponding to the outermost Region 3. On the other hand, leaky-waves are produced by non-spectral poles that are present in the lower Riemann sheet. It had been noted earlier that the space-wave radiation patterns are plotted by considering the azimuthal summation over n in the range -20 - 20 . The high directivity in the space-wave radiation is contributed by a particular dominant n in the above range, with the non-dominant radiation in other directions due to other values of n . Poles in the leaky-wave radiation corresponding to this

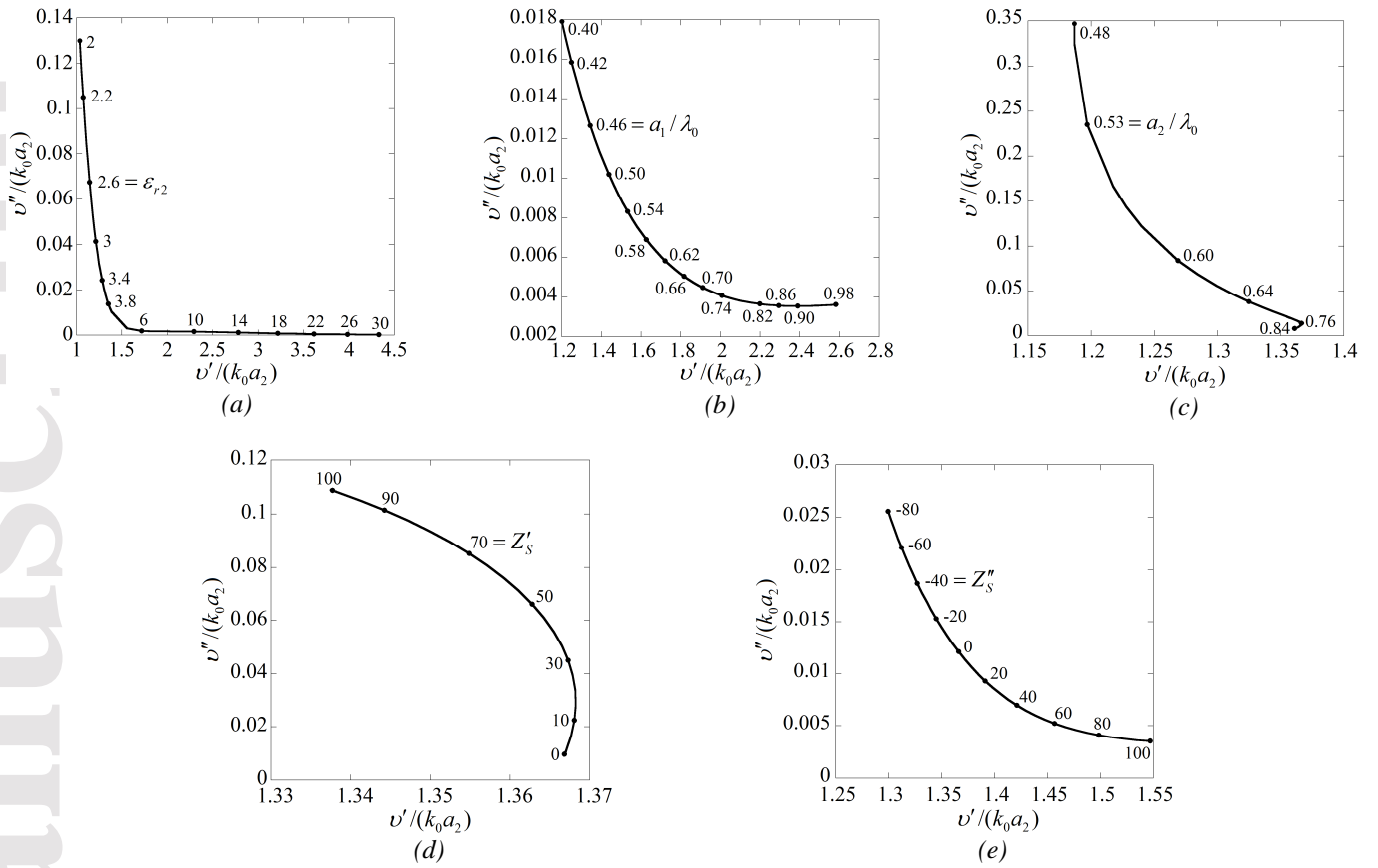


Fig. 9. Normalized creeping-wave pole loci in the complex v -plane for $\hat{\phi}$ -directed electric source excitation with variation in (a) ϵ_{r2} : $a_1 = 0.47\lambda_0$, $a_2 = 0.74\lambda_0$, $Z_s = (1+1j)\Omega$, (b) a_1/λ_0 : $\epsilon_{r2} = 3.9$, $a_2 - a_1 = 0.27\lambda_0$, $Z_s = (1+1j)\Omega$, (c) a_2/λ_0 : $\epsilon_{r2} = 3.9$, $a_1 = 0.47\lambda_0$, $Z_s = (1+1j)\Omega$ (d) $Z'_s (\Omega)$: $\epsilon_{r2} = 3.9$, $a_1 = 0.47\lambda_0$, $a_2 = 0.74\lambda_0$, $Z''_s = 1\Omega$ and (e) $Z''_s (\Omega)$: $\epsilon_{r2} = 3.9$, $a_1 = 0.47\lambda_0$, $a_2 = 0.74\lambda_0$, $Z'_s = 1\Omega$.

dominant n are found to be non-spectral that contributes to leaky-wave radiation. However, when the leaky-wave pole is not dominant (corresponding to higher attenuation constants for the leaky-wave), the space-wave radiation dominates over the leaky-wave radiation. The excellent agreement discussed in the manuscript between the theoretical and simulated results of course is despite the small difference between the theoretical and simulated results below -20 dB, that contributes to part of the non-dominant radiation.

6.3. Creeping-wave

The dominant contribution to the creeping-waves for the configuration correspond to poles with a low attenuation constant v'' obtained from $G_1 = 0$ for excitation with the $\hat{z}/\hat{\rho}$ -directed sources and for $G_2 = 0$ for excitation with the $\hat{\phi}$ -directed source for $n = v$. A pole is associated with the leaky-wave, creeping-wave or trapped-wave depending on its location in the complex v -plane. Particularly, the conditions $v' < k_0 a_2$, $v' \approx k_0 a_2$ or $v' > k_0 a_2$ correspond to the leaky-wave, creeping-wave and trapped-waves, respectively [26], [27]. The trapped-wave (Elliott modes), are slow-waves propagating within the dielectric layer in Region 2, characterized by low attenuation rates. The

creeping-waves (Watson modes) possess higher attenuation rates compared to the trapped-modes.

The normalized creeping-wave pole loci with variation in the design parameters is plotted in Fig. 8 and 9 for excitation with the $\hat{z}/\hat{\rho}$ - and the $\hat{\phi}$ -directed sources, respectively. Figs. 8(a) and 9(a) demonstrate the effect of the variation in coating permittivity on the normalized creeping-wave pole. It is observed that normalized attenuation constant decreases sharply with a small change in the normalized phase constant for $2 \leq \epsilon_{r2} \leq 6$, corresponding to creeping-wave, with the waves trapped inside the dielectric for $\epsilon_{r2} > 6$ with a very small attenuation constant. The permittivity $\epsilon_{r2} = 6$ corresponds to the transition between the creeping-wave and the trapped-wave. It can thus be observed that for a higher coating permittivity, surface-waves propagate circumferentially with very small attenuation constants.

The normalized creeping-wave pole loci with variation in the radius of the impedance cylinder is shown in Figs. 8(b) and 9(b). It is observed that for $a_1 > 0.78\lambda_0$ and $a_1 > 0.50\lambda_0$ for the $\hat{z}/\hat{\rho}$ - and the $\hat{\phi}$ -directed sources respectively, the surface-waves are trapped inside the dielectric with reduction in the attenuation constants, while for lower radii of the impedance cylinder, the waves are creeping in nature with increase in attenuation constant.

However, a much stronger effect on the attenuation constant is observed with the variation in the radius of the dielectric coating in Figs. 8(c) and 9(c), with a significant reduction in the attenuation constant with increasing coating thickness both for the $\hat{z}/\hat{\rho}$ - and the $\hat{\phi}$ -directed sources. It is observed that surface-waves with very low attenuation are trapped in the dielectric layer for $a_2 > 0.78\lambda_0$ corresponding to both the $\hat{z}/\hat{\rho}$ - and $\hat{\phi}$ -directed sources, with the dielectric coating radius $a_2 = 0.78\lambda_0$ at the transition between the creeping-wave and trapped-wave.

The normalized creeping-wave pole-loci with variation in the real part of the surface impedance is shown in Figs. 8(d) and 9(d). An enhancement in the attenuation constant is observed with increase in Z'_s irrespective of the source polarizations, with the phase constant increasing/decreasing with increase in Z'_s for the $\hat{z}/\hat{\rho}$ - and the $\hat{\phi}$ -directed sources, respectively. Figs. 8(e) and 9(e) show the effect on the propagation characteristics with variation in the imaginary part of the surface impedance. It can be observed from both Figs. 8(e) and 9(e) that creeping-waves are more strongly excited by an inductive surface impedance compared to a capacitive surface impedance for excitation with both the $\hat{z}/\hat{\rho}$ - and the $\hat{\phi}$ -directed sources.

7. Conclusion

The dielectric coated impedance cylinder configuration is investigated rigorously with respect to the space-wave, leaky-wave and creeping-wave excitations for all source polarizations. It is observed that compared to the dielectric cylinder configuration investigated earlier, a much higher directivity is achieved for the space-wave and leaky-waves for the current antenna configuration. The large enhancement of leaky-wave directivity is due to the non-spectral poles contributed by the term $(\bar{\mathbf{I}} - \bar{\mathbf{R}}_{21} \cdot \bar{\mathbf{R}}_{23})$ in the current configuration compared to the poles due to the transmission matrix $\bar{\mathbf{T}}_{12}$ in [13] for the homogeneous cylindrical rod antenna radiating in free-space. In addition, the dominant leaky-wave poles corresponding to minimum attenuation is observed to occur for higher-order azimuthal harmonics instead of $n=0$ for the case of the homogeneous dielectric cylinder. The design parameter values for the antenna configuration are optimized to maximize the antenna directivity for the space-wave and leaky-wave cases. For the leaky-wave excitation, the phase and attenuation characteristics are used to evaluate the proper leaky-wave region with the azimuthal harmonic corresponding to the dominant leaky-mode excitation with high directivity. The radiation characteristics for dominant leaky-mode harmonic show that a very high directivity can be obtained from the antenna configuration corresponding to an appropriate azimuthal harmonic and optimized structural parameter. A very high space-wave directivity is also observed for the current antenna configuration compared to the cylindrical rod antenna in [13] that is contributed by higher-order azimuthal harmonics in the current case compared to lower-order space-wave harmonics in [13]. The propagation characteristics of the creeping-waves are also examined. It is observed that the creeping-wave poles in the current

configuration are dependent on the source-polarization as contrasted to the homogeneous dielectric cylinder where they are independent of the source orientation. The creeping-waves are also observed to be more strongly excited by an inductive surface-impedance compared to a capacitive surface-impedance for all source-polarizations with the thickness of the dielectric coating significantly affecting the creeping-wave attenuation characteristics.

8. References

- [1] P. S. Carter, "Antenna arrays around cylinders," *Proc. IRE*, vol. 31, no. 12, pp. 671–693, Dec. 1943.
- [2] C. H. Papas, "Diffraction by a cylindrical obstacle," *J. Appl. Phys.*, vol. 21, no. 4, pp. 318–325, Apr. 1950.
- [3] W. S. Lucke, "Electric dipoles in the presence of elliptic and circular cylinders," *J. Appl. Phys.*, vol. 22, no. 1, pp. 14–19, Jan. 1951.
- [4] J. R. Wait, *Electromagnetic Radiation from Cylindrical Structures*. New York, NY, USA: Pergamon, 1959.
- [5] J. R. Wait, "Scattering of a plane wave from a circular dielectric cylinder at oblique incidence," *Can. J. Phys.*, vol. 33, no. 5, pp. 189–195, May 1955.
- [6] R. Lytle, "Far-field patterns of point sources operated in the presence of dielectric circular cylinders," *IEEE Trans. Antennas Propag.*, vol. 19, no. 5, pp. 618–621, Sep. 1971.
- [7] D. R. Jackson and N. Alexopoulos, "Gain enhancement methods for printed circuit antennas," *IEEE Trans. Antennas Propag.*, vol. 33, no. 9, pp. 976–987, Sep. 1985.
- [8] H. Yang and N. Alexopoulos, "Gain enhancement methods for printed circuit antennas through multiple superstrates," *IEEE Trans. Antennas Propag.*, vol. 35, no. 7, pp. 860–863, Jul. 1987.
- [9] D. R. Jackson and A. A. Oliner, "A leaky-wave analysis of the high-gain printed antenna configuration," *IEEE Trans. Antennas Propag.*, vol. 36, no. 7, pp. 905–910, Jul. 1988.
- [10] D. R. Jackson, A. A. Oliner and A. Ip, "Leaky-wave propagation and radiation for a narrow-beam multiple-layer dielectric structure," *IEEE Trans. Antennas Propag.*, vol. 41, no. 3, pp. 344–348, Mar. 1993.
- [11] J. W. Duncan, "The efficiency of excitation of a surface-wave on a dielectric cylinder," *IRE Trans. Microw. Theory Techn.*, vol. 7, no. 2, pp. 257–268, Apr. 1959.
- [12] R. Paknys and D. R. Jackson, "The relation between creeping-waves, leaky-waves, and surface-waves," *IEEE Trans. Antennas Propag.*, vol. 53, no. 3, pp. 898–907, Mar. 2005.
- [13] M. Singh, B. Ghosh and K. Sarabandi, "Excitation of space-wave, leaky-wave and creeping-waves in cylindrical media," *IEEE Trans. Antennas Propag.*, vol. 66, no. 12, pp. 7100–7110, Dec. 2018.
- [14] L. C. Lin, H. Miyagawa, T. Kitazawa, R. B. Hwang and Y. D. Lin, "Characterization and design of cylindrical microstrip leaky-wave antennas," *IEEE Trans. Antennas Propag.*, vol. 56, no. 7, pp. 1853–1859, Jul. 2008.
- [15] K. Sarabandi, M. D. Casciato, and I. S. Koh, "Efficient calculation of the fields of a dipole radiating above an

- impedance surface,” *IEEE Trans. Antennas Propag.*, vol. 50, no. 9, pp. 1222–1235, Sep. 2002.
- [16] H. Mosallaei and K. Sarabandi, “Antenna miniaturization and bandwidth enhancement using a reactive impedance substrate,” *IEEE Trans. Antennas Propag.*, vol. 52, no. 9, pp. 2403–2414, Sep. 2004.
- [17] C. Tokgoz and R. J. Marhefka, “A UTD based asymptotic solution for the surface magnetic field on a source excited circular cylinder with an impedance boundary condition,” *IEEE Trans. Antennas Propag.*, vol. 54, no. 6, pp. 1750–1757, Jun. 2006.
- [18] A. Illahi, Q. A. Naqvi, and K. Hongo, “Scattering of dipole field by a finite conducting and a finite impedance cylinder,” *Progress In Electromagnetics Research M*, vol. 1, pp. 139–184, 2008.
- [19] A. G. Aguilar, Z. Sipus and M. Sierra-Pérez, “An asymptotic solution for surface fields on a dielectric-coated circular cylinder with an effective impedance boundary condition,” *IEEE Trans. Antennas Propag.*, vol. 61, no. 10, pp. 5175–5183, Oct. 2013.
- [20] A. G. Aguilar, P. H. Pathak and M. Sierra-Perez, “A canonical UTD solution for electromagnetic scattering by an electrically large impedance circular cylinder illuminated by an obliquely incident plane wave,” *IEEE Trans. Antennas Propag.*, vol. 61, no. 10, pp. 5144–5154, Oct. 2013.
- [21] W. C. Chew, *Waves and Fields in Inhomogeneous Media*. New York, NY, USA: IEEE Press, 1995.
- [22] T. B. A. Senior and J. L. Volakis, *Approximate Boundary Conditions in Electromagnetics*. London: IEE Press, 1995.
- [23] R. F. Harrington, *Time Harmonic Electromagnetic Fields*. New York, NY, USA: McGraw-Hill, 1961.
- [24] A. Ishimaru, *Electromagnetic Wave Propagation, Radiation, and Scattering*. Englewood Cliffs, NJ, USA: Prentice-Hall, 1991.
- [25] *HFSS Version 13.0*. Ansoft Corporation, Pittsburgh, PA, USA, 2010.
- [26] K. Naishadham and L. B. Felsen, “Dispersion of waves guided along a cylindrical substrate-superstrate layered medium,” *IEEE Trans. Antennas Propag.*, vol. 41, no. 3, pp. 304–313, Mar. 1993.
- [27] K. Naishadham and J. E. Piou, “Analytical characterization and validation of creeping-waves on dielectric coated and perfectly conducting cylinders,” *Radio Sci.*, vol. 45, no. 5, pp. 1–19, Oct. 2010.